# Formation and preservation of greigite ($Fe_3S_4$) in sediments from the Santa Barbara Basin: Implications for paleoenvironmental changes during the past 35 ka

C. L. Blanchet,[1,2] N. Thouveny,[1] and L. Vidal[1]

[1] Diagenetic processes are known to modify sedimentary records, but they can also reveal important paleoenvironmental changes. Here we investigate variations in sedimentary iron diagenesis and depositional environments for the last 35 ka by analyzing the rock magnetic and geochemical properties of two sediment cores collected in the Santa Barbara Basin (California). In organic-rich sediments, early diagenesis often leads to partial dissolution of detrital iron oxides and stepwise formation of authigenic pyrite ($FeS_2$). The pyritization process takes place following several geochemical pathways, sometimes involving intermediate iron sulfide species such as greigite ($Fe_3S_4$). Sedimentary conditions in the basin appear to have recurrently favored preservation of greigite (identified by its magnetic properties) and inhibited its complete transformation into pyrite. The Holocene interval contains a series of centimeter-thick greigite-bearing layers that are associated with large flood deposits, which are known in the basin as "gray layers." We propose that greigite preservation was enabled in these sediments by their relative enrichment in reactive iron over organic matter and/or hydrogen sulfide (because of their high ratio of terrigenous over organic material), which limited pyritization reactions. Within the glacial deposits, formation and preservation of meter-thick greigite layers occurred in terrigenous-rich and organic-poor sedimentary layers and is proposed to result from a similar diagenetic process to that in the Holocene greigite-bearing layers (dominance of reactive iron over organic matter and/or $HS^-$). The terrigenous enrichments in the glacial greigite-bearing layers are probably related to climatic or sea level changes because they occur at times of massive iceberg releases in the North Atlantic, the so-called Heinrich events.

## 1. Introduction

[2] The sediments deposited in the Santa Barbara Basin (California, USA) have been intensively studied to reconstruct climatic and oceanographic changes on seasonal to orbital time scales [e.g., *Behl and Kennett*, 1996]. In the basin, sedimentary dynamics are extremely sensitive to fluctuations in sea level, and climatic and oceanic regimes, because of its proximity to the American continent, its sill-shaped structure and a complex oceanic context [*Behl*, 1995; *Ingram and Kennett*, 1995].

[3] Water masses in the Santa Barbara Basin (SBB) are currently characterized by a strong bathymetric oxygenation gradient, which results in suboxic conditions at the bottom of the basin. In the deeper parts of the basin, bioturbation is inhibited and seasonal deposits are preserved as millimeter-thick laminations. A 200-m long Ocean Drilling Program (ODP) core (Site 893) contains an alternating sequence of laminated and bioturbated sediments that documents large variations in past depositional environments. Different sedimentary facies, identified by their degree of bioturbation and by their benthic assemblage, are related to varying bottom water oxygenation [*Behl*, 1995]. Oxygenation conditions rapidly responded to glacial/interglacial and Dansgaard-Oeschger climatic fluctuations [*Behl and Kennett*, 1996; *Cannariato et al.*, 1999]. Past oceanic circulation and hydrologic conditions have followed the same pacing [*Hendy and Kennett*, 1999; *Emmer and Thunell*, 2000; *Pospelova et al.*, 2006]. Continental climatic changes have received less attention, although vegetation changes [*Heusser*, 1998] and glacial advances [*Phillips et al.*, 1996] indicate different responses. Vegetation changes seem to be related to Dansgaard-Oeschger fluctuations, while the glacial advances appear to have occurred at the times of Heinrich events (massive iceberg releases in the North Atlantic [*Bond et al.*, 1992]). The effect of continental climatic changes on the strength of erosion and on the rhythm of sediment delivery to the marine realm remains poorly explored.

[4] In order to trace changes in terrigenous input, we measured the magnetic properties of two sedimentary sequences collected during the IMAGESVIII-MONA cam-

[1]CEREGE, Université Paul Cézanne, Aix en Provence, France.
[2]Now at Leibnitz Institute of Marine Sciences at University of Kiel (IFM-GEOMAR), Kiel, Germany.

**(a) Eastern Pacific OMZ**

**(b) Water column: Seasonal O₂**
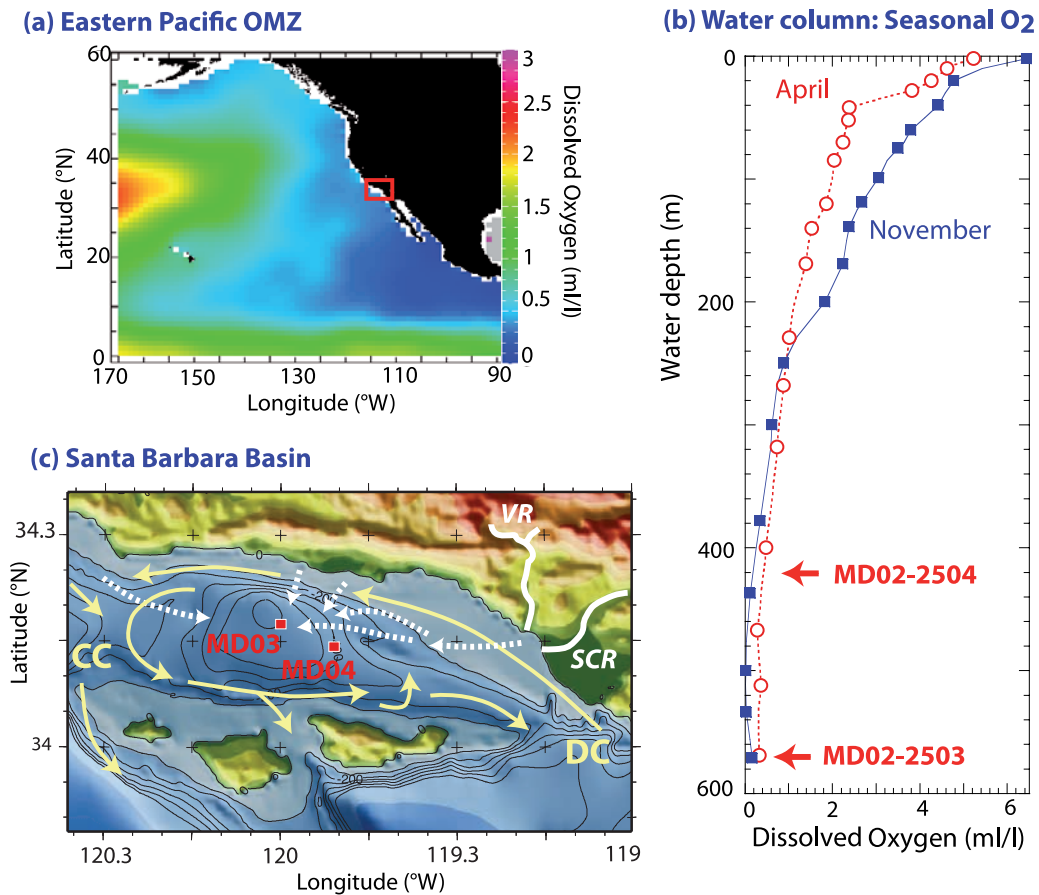
**(c) Santa Barbara Basin**

**Figure 1.** Present-day climatic and oceanographic regimes in the Santa Barbara Basin. (a) Oxygen minimum zone (OMZ) of the eastern Pacific: dissolved oxygen content (mL/L) at 700 m water depth (Word Ocean Atlas [*Conkright et al.*, 2002]). Spatial extension of the O₂-depleted waters depicted by blue colors. (b) Profiles of dissolved oxygen in the water column of the Santa Barbara Basin in April and November 2007 (34.16°N, 120°W [*CalCOFI*, 2007a, 2007b]) and water depths of the studied cores with respect to the profile. (c) Map of the Santa Barbara Basin (GEBCO Atlas), with location of the cores, surface currents (yellow solid arrows: CC, California Current; DC, Davidson Current), rivers (white solid lines: VR, Ventura River; SCR, Santa Clara River), and sediment transportation routes (white dotted arrows).

paign (R/V *Marion Dufresne*, 2002 [*Beaufort et al.*, 2002]). Rock magnetic parameters provide useful information about variations in the concentration and mineralogy of detrital (oxyhydr)oxide minerals, which are tracers of sediment sources and transport mechanisms [*Bloemendal et al.*, 1993; *Moreno et al.*, 2002; *Köhler et al.*, 2008]. However, the magnetic signature of the deposited detrital minerals can be significantly altered by the formation of authigenic iron sulfides. Widespread in marginal organic-rich sediments, the pyritization process leads to progressive dissolution of iron oxides and stepwise formation of pyrite ($FeS_2$). In sediments from the Californian margin, accumulations of greigite ($Fe_3S_4$) have been detected by its magnetic properties [*Leslie et al.*, 1990; *Rowan et al.*, 2009]. This mineral is an intermediate sulfide species, and is metastable with respect to pyrite. It is frequently preserved in the geological record as a result of specific geochemical/depositional environment (e.g., dominance of reducible iron oxyhydroxide minerals over reactive organic matter) [*Berner*,

1984; *Kasten et al.*, 2003; *Kao et al.*, 2004; *Roberts and Weaver*, 2005; *Fu et al.*, 2008]. The aim of our study is to reconstruct the sedimentary dynamics in the SBB, in order to (1) characterize variations in terrigenous input during the past 35 ka and (2) investigate the potential influence of changes in sedimentary composition on ferrimagnetic iron sulfide growth and preservation.

## 2. Sedimentary Environment and Core Description

### 2.1. Hydrologic and Climatic Settings

[5] The intermediate water masses that flow between water depths of 300 and 800 m along the western North American margin are strongly depleted in dissolved oxygen (0.3–1.4 mL $O_2$/L [*California Cooperative Oceanic Fisheries Investigations* (*CalCOFI*), 2005]), which defines the oxygen minimum zone (OMZ) of the eastern Pacific (Figure 1a). In the SBB, the oxygenation gradient follows

seasonal variations in oceanic circulation and primary productivity [*Reimers et al.*, 1990]. In spring, the bottom waters (BW) have relatively high oxygen and nitrate contents ($\sim$0.2 mL $O_2$/L (Figure 1b)) because cold, oxygenated and nutrient-rich waters flow into the deep basin. The surface waters are cold and rich in chlorophyll because of upwelled nutrient-rich and cold BW, which stimulate primary productivity. During summer, the BW gradually become less oxygenated because of the degradation of sinking organic matter and they remain suboxic in fall and winter (<0.1 mL $O_2$/L (Figure 1b)).

[6] The cold southward flowing Californian Current (CC) and the warm northward flowing Davidson Current (DC) seasonally prevail at the surface in the basin (Figure 1c): during spring and summer, a high-pressure cell over the North Pacific favors the CC, imposing dry weather on the Californian coast. During fall and winter, a low-pressure cell over the Gulf of Alaska favors the DC, which generates large rainfalls on the Californian margin [*Conil and Hall*, 2006].

## 2.2. Current Sedimentation

[7] The strong seasonality of the local climatic and oceanographic regimes leads to seasonal modulation of terrigenous and biogenic inputs to the basin. In winter, sedimentation is mainly fed by terrigenous inputs, transported by rivers (the Santa Clara and Ventura rivers on the southeastern margin (Figure 1c)) and winds (Santa Ana winds [*Westerling et al.*, 2004]). In spring and summer, sedimentation mainly consists of diatoms and foraminifera, with productivity being favored by upwelling [*Bull and Kemp*, 1995]. In the anoxic part of the basin, this seasonal signal is preserved as millimeter-thick laminae [*Soutar and Crill*, 1977; *Reimers et al.*, 1990].

[8] Pore water and solid phase geochemical profiles from several sediment cores collected at different locations and seasons at the bottom of the SBB are similar [*Reimers et al.*, 1996; *Kuwabara et al.*, 1999]. This allows a regional picture to be drawn of diagenetic processes within superficial sediments of the SBB. The oxygen content of the pore waters follows seasonal changes in bottom water oxygenation: oxygen diffuses $\sim$4 mm beneath the seafloor when the BW are oxygenated (in spring), but it does not penetrate when the BW are anoxic (in fall or winter). $NO_3^-$, $Mn^{2+}$, $Fe^{2+}$ and $\sum H_2S$ profiles seem to be unaffected by seasonal variations of bottom water chemistry. The three former species are detected in the uppermost 3 cm of the sediment column (and $Fe^{2+}$ until 6 cm) and the latter is detected below 4 cm. Formation of solid phase iron sulfides in the upper zone of the sediment column is indicated by low dissolved sulfide content in the uppermost 4 cm (despite high rates of sulfate reduction) and a large enhancement of $H_2S$ coinciding with $Fe^{2+}$ depletion [*Reimers et al.*, 1996]. The sulfate-methane transition zone is identified by codepletion of $SO_4^{2-}$ and $CH_4$ between 150 and 200 cm below seafloor in various studies [*Barnes and Goldberg*, 1976; *Reimers et al.*, 1996].

## 2.3. Description of the Cores

[9] Two sediment cores from the SBB were analyzed for this study: core MD02-2503 (34.17°N, 120.02°W) from the

bottom of the basin (596 m water depth) and core MD02-2504 (34.14°N, 119.52°W) from the eastern sill (425 m water depth) (Figures 1b and 1c). Both cores contain alternations of foraminifera-rich silty clays and siliceous mud that range in color from dark gray to dark olive green, with millimeter-scale laminae forming couplets or triplets. In the upper 15 m of both cores, centimeter-thick gray-colored silty layers are observed, sometimes with sharp bases and upward fining. They are more numerous in the deeper core MD02-2503.

[10] In this core, the laminations dominate two major zones (the upper 15 meters and the 18–21 m interval) and occur in a few thinner intervals (34, 38, 39, 43.3–44 and 45 m) (Figure 2b). In core MD02-2504, the laminations only appear between 15 and 19 m and at $\sim$36 m (Figure 2c). Elsewhere, the hemipelagic clays are homogeneous with varying degrees of bioturbation.

## 3. Methods
### 3.1. Magnetic Properties

[11] Magnetic parameters were measured at the CEREGE laboratory (Aix en Provence), at 2-cm stratigraphic intervals on U channel samples (1.5 m long, 4 $cm^2$ section) subsampled from the cores after a few months of storage at 4°C. The volume magnetic susceptibility ($\kappa$, in $10^{-5}$ SI) was measured using a pass-through MS2-B loop sensor connected to a Bartington Instruments MS2 magnetic susceptibility meter. Two types of artificially induced remanent magnetization were imparted: (1) an anhysteretic remanent magnetization (ARM) was produced in a 100 mT alternating field (peak amplitude) with a superimposed 0.1 mT steady field and (2) two isothermal remanent magnetizations ($IRM_{1T}$ and $IRM_{-0.3T}$) were imparted by passing the U channels through two different Halbach cylinders (permanent rare earth magnets) that develop fields of 1 T and 0.3 T, respectively [*Rochette et al.*, 2001]. Remanent magnetizations were measured using a superconducting quantum interference device (SQUID) pass-through magnetometer (2G 760R, located in a shielded room). The response curves of the SQUIDs integrate widths of $\sim$4 cm for the $x$ and $y$ axes and $\sim$6 cm for the z axis, producing a slight smoothing of the signals [*Weeks et al.*, 1993]. Stepwise alternating field (AF) demagnetization was performed at peak fields of 5, 10, 15, 20, 25, 30, 40, 50, 60 and 80 mT. Magnetizations are expressed in volume magnetizations (A/m).

[12] Discrete samples were collected at several depth intervals for complementary rock magnetic analyses. Isothermal remanent magnetizations were imparted in a 9 T field ($IRM_{9T}$) using a pulse magnetizer (Magnetic Measurements Ltd., model MMPM9) and were thermally demagnetized in an argon atmosphere (furnace model Magnetic Measurements Ltd. MMTD1, located in a shielded room). Temperatures were increased at 100°C steps from 100 to 500°C (with an intermediate step at 350°C) and at 30°C steps from 500 to 680°C. Hysteresis loops were measured to ±1 T and demagnetization of the $IRM_{1T}$ was performed on selected samples with an alternating gradient magnetometer (Princeton Measurements Corporation, model Micromag 3900).
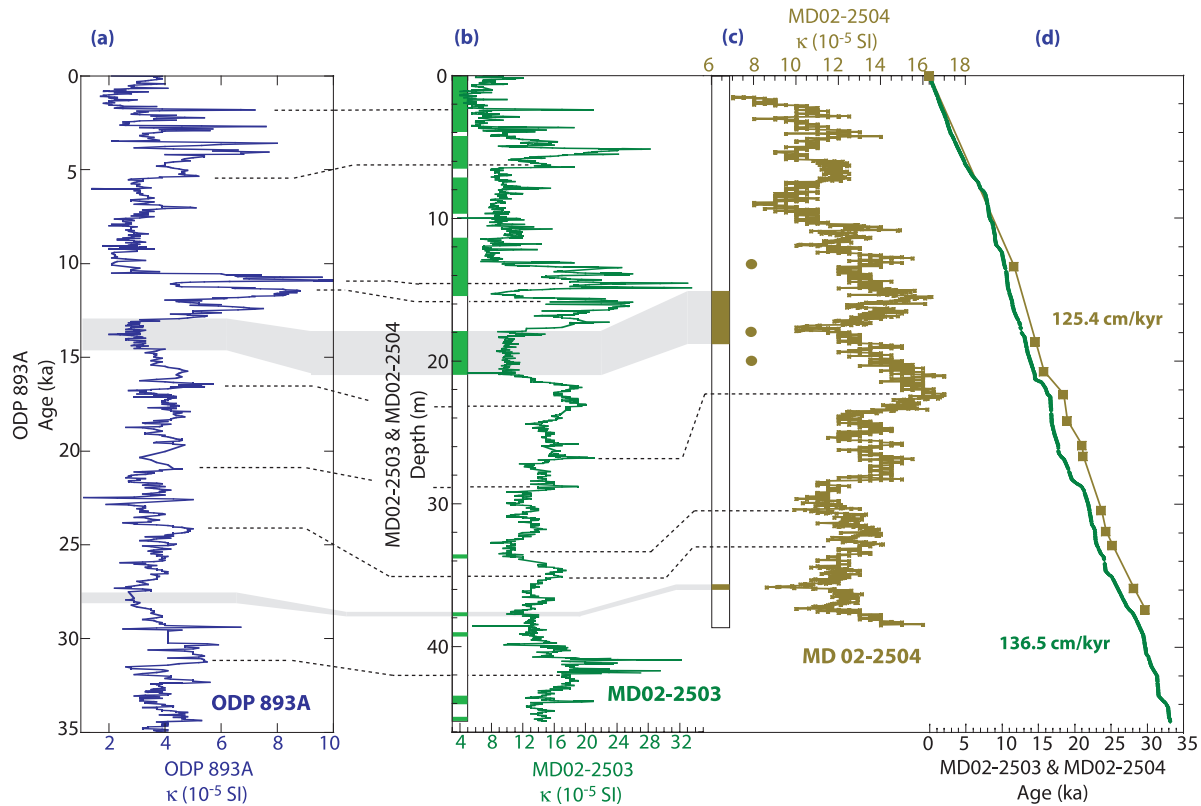
**Figure 2.** Chronostratigraphy for cores MD02-2503 and MD02-2504. (a) Magnetic susceptibility profile for ODP Hole 893A [*Rack et al.*, 1995] on the age scale constructed by *Ingram and Kennett* [1995] and *Hendy et al.* [2002]. Magnetic susceptibility profiles for (b) core MD02-2503 and (c) core MD02-2504 on their respective depth scales. (d) Age-depth correlation performed using the software Analyseries [*Paillard et al.*, 1996]. Three dated points (dots) determined by *Hill et al.* [2006] help to constrain the age model of core MD02-2504. Mean sedimentation rates are indicated for the two MD cores.

[13] Low-temperature (300 to 5 K) measurements of IRM$_{5T}$ were performed on a Magnetic Properties Measurement System (MPMS-XL7) at the University of Bremen on discrete samples. An IRM imparted in a 5 T field at 300 K (IRM$_{5T}$) was measured during cooling (down to 5 K) and warming (up to 300 K).

### 3.2. Bulk Elemental Contents

[14] Bulk major and trace element concentrations were semiquantitatively estimated using an X-ray fluorescence scanner (XRF, Avaatech$^{TM}$) at the MARUM-Center for Marine Environmental Sciences (University of Bremen). Measurements were performed on the U channels from core MD02-2503, at 2-cm intervals over an area of 1 cm$^2$. The technical basis for XRF scanning measurements is described by *Richter et al.* [2006]. For our study, the settings were adjusted at 10 kV in order to detect aluminum (Al), titanium (Ti), silicon (Si), calcium (Ca), sulfur (S), potassium (K) and iron (Fe). Results are provided in counts/s. Although this method allows rapid measurement of elemental contents along sediment cores, the semiquantitative results must be validated by determination of absolute elemental content from discrete samples. The absolute quantities of elements ranging from magnesium (Mg) to

barium (Ba) were therefore measured on 26 discrete samples collected from the archive halves of the cores and from the U channel samples from core MD02-2503 using an energy dispersive polarization XRF analyzer (EDP-XRF Spectro XEPOS) at the University of Bremen. Technical information concerning the reproducibility and accuracy of this instrument is provided by *Wien et al.* [2005]. Results are given in g/kg. Problems concerning the conversion of relative to absolute elemental concentrations, the origin of potential mismatches (e.g., different sample size and preparation, slight shifts in sample depths) and use of adequate statistical treatments have been tackled by *Weltje and Tjallingii* [2008].

### 4. Chronostratigraphy

[15] The chronology for core MD02-2503 was derived from that of ODP Site 893A using a core-to-core correlation based on the magnetic susceptibility profiles (Figure 2). The ODP Site 893A magnetic susceptibility record was produced by *Rack et al.* [1995] and the age model was established by *Ingram and Kennett* [1995] and refined by *Hendy et al.* [2002] on the basis of $^{14}$C ages and correlation points to the $\delta^{18}$O record of the GISP2 Greenland ice core
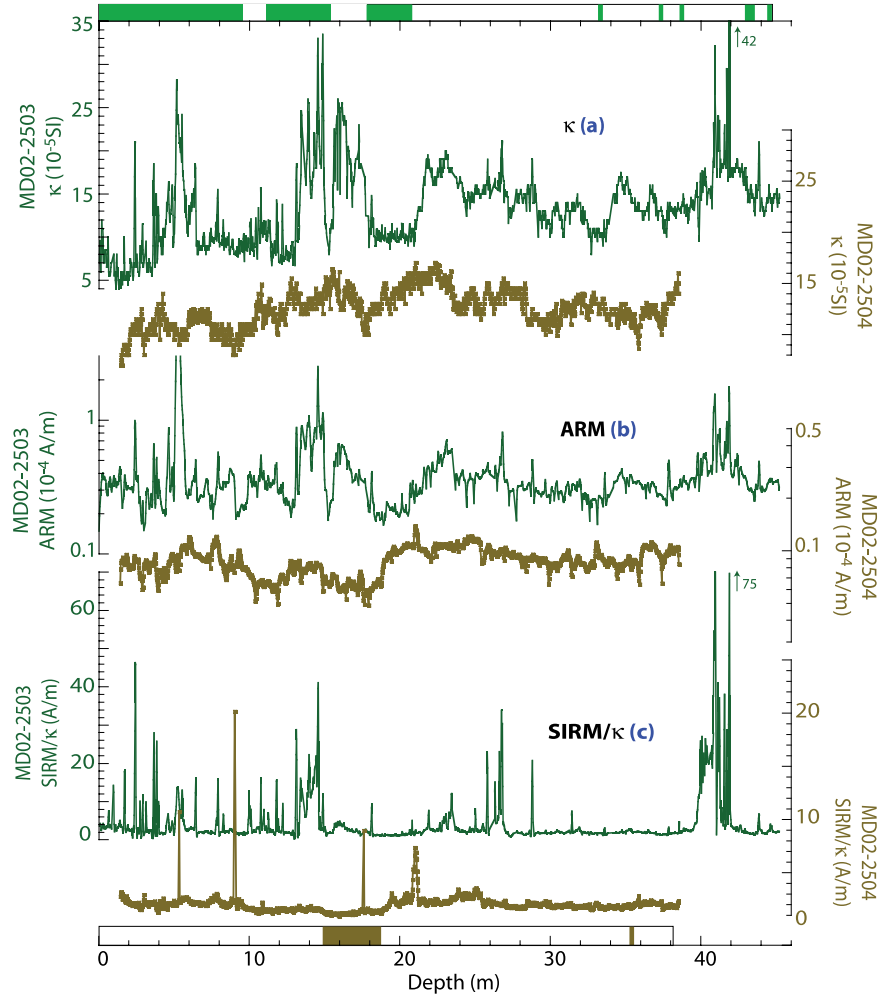
**Figure 3.** Depth variations of magnetic parameters for cores MD02-2503 and MD02-2504. (a) Magnetic susceptibility ($\kappa$) and (b) anhysteretic remanent magnetization (ARM) (on a logarithmic scale) indicate variations in magnetic mineral concentration. (c) The ratio of saturation isothermal remanent magnetization imparted at 1 T (SIRM) over magnetic susceptibility (SIRM/$\kappa$) is an indicator of fine grain material. Ferrimagnetic iron sulfides typically occur in the single-domain state, as indicated by peaks in SIRM/$\kappa$ [*Roberts*, 1995]. Laminated intervals are indicated by colored rectangles.

[*Grootes and Stuiver*, 1997]. Slight differences between the two profiles result from different resolution, sensitivity and calibration between the susceptibility probes used for the different measurements (a Bartington Instruments MS2C point sensor for the ODP core and a pass-through Bartington Instruments MS2B loop sensor for the MD cores). The chronology for core MD02-2504 was established by (1) correlation of *Globigerinoides bulloides* $\delta^{18}$O record to the GISP2 $\delta^{18}$O record [*Hill et al.*, 2006] for the upper 25 m of the core and (2) correlation of $\kappa$ profiles from cores MD02-2504 and MD02-2503, particularly between 25 and 40 m (Figure 2). Depth-to-age transformation was obtained by linear interpolation between each dated level and reveals that cores MD02-2503 and MD02-2504 cover the intervals 0–33 ka and 0–30 ka, respectively (Figure 2). Their mean sedimentation rates are nearly constant and similar (136 cm/ka for MD02-2503 and 125 cm/ka for MD02-2504). Some of

the laminated intervals in the two cores correspond to the same time intervals (i.e., between 13 and 15 ka and at 28 ka (Figure 2)). The temporal resolution of the magnetic and elemental profiles is ~15 years.

## 5. Results

### 5.1. Rock Magnetic Measurements

[16] Rock magnetic profiles for cores MD02-2503 and MD02-2504 are characterized by a series of large-amplitude spikes (Figure 3). The two cores have similar range of magnetic susceptibility values (from 4 to 42.10$^{-5}$ SI) and similar long-term trends, with higher values in the 22–46 m interval than in upper 20 m (Figure 3a). Magnetic susceptibility spikes mainly occur in core MD02-2503, at 2–6 m, 13–18 m and 40–42 m. Both ARM profiles have similar long-term trends but the ARM values in core MD02-2504 are lower than in core MD02-2503 (Figure 3b). In core
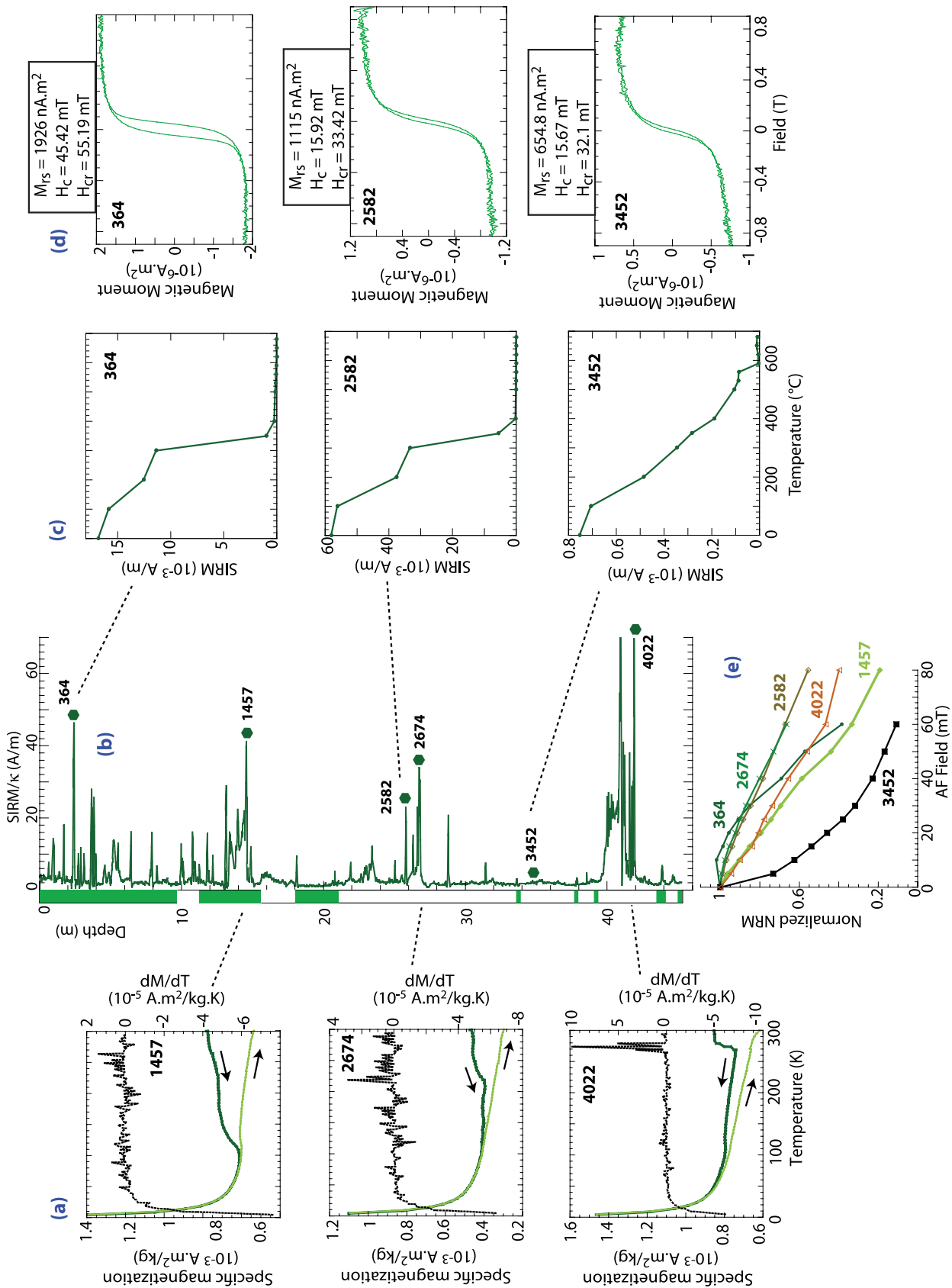
**Figure 4**

MD02-2503, most SIRM/$\kappa$ values range between 2 and 10 A/m with sharp spikes up to 75 A/m occurring as thick intervals (e.g., at 13–15 m and 40–42 m) or as sharp spikes (e.g., in the upper 12 m, at 18 m and 26 m) (Figure 3c). In core MD02-2504, spikes of smaller amplitude (up to 20 A/m) occur in the SIRM/$\kappa$ record at 5 m, 9 m, 17.5 m and 21 m (Figure 3c). In both cores, SIRM profiles are very similar to SIRM/$\kappa$ records. In core MD02-2503, higher HIRM and lower S ratio are associated to SIRM/$\kappa$ peaks. The ratio $ARM_{AF30mT}/ARM$ for core MD02-2503 also have sharp spikes in association with the SIRM/$\kappa$ peaks. In contrast, the ARM/$\kappa$ values are not higher in the SIRM/$\kappa$ peaks.

[17] Complementary information has been derived from thermal demagnetization of the $IRM_{9T}$ and hysteresis measurements of samples from core MD02-2503 (Figure 4). A steep loss of $IRM_{9T}$ occurs between 300 and 350°C for samples from the high-SIRM/$\kappa$ layers, whereas the $IRM_{9T}$ demagnetization is more gradual and decays to zero between 560 and 590°C for samples from low-SIRM/$\kappa$ layers (i.e., background sediments (Figure 4c)). High-SIRM/$\kappa$ layers have high coercivity ($H_c$ and $H_{cr}$), high saturation magnetization ($M_{rs}$) and high saturation field ($H_{sat} > 0.2$ T) (Figure 4d). Low-temperature $IRM_{5T}$ cooling curves undergo a major decrease between 270 and 220 K and converge with the warming curves at ∼100–120 K (Figure 4a). High-SIRM/$\kappa$ layers have higher natural remanent magnetization (NRM) unblocking fields than the background sediments (Figure 4e).

## 5.2. Elemental Content Measurements

[18] Stratigraphic variations of relative elemental concentrations along core MD02-2503 are depicted using log ratios in order to avoid dilution effects (green curves in Figure 5). They are compared to log ratios of absolute elemental content (yellow squares in Figure 5) and their relationships are explored using linear regressions [*Weltje and Tjallingii*, 2008]. Relative variations of Fe, Ti, K, Al and Ca are used to provide a synoptic view of changes in sediment composition. Fe, Ti, K and Al are contained mostly in terrigenous silicates and oxides. However, Fe is dissolved easily and can be integrated into authigenic iron sulfides or phosphates. Ca has been shown to be mainly related to biogenic carbonate production in the Santa Barbara Basin [*Gardner and Dartnell*, 1995; *Reimers et al.*, 1996]. Therefore, the Ca/Al ratio provides an estimation of changes in the biogenic/terrigenous contributions. Ratios Fe/Ti and Fe/K provide information about changes in mineralogy of the terrigenous fraction and/or diagenetic processes involving Fe (e.g., dissolution, migration and recrystallization). The correlation coefficient is significant for Ca/Al ($R^2 = 0.68$ (Figure 5a)), poorly

significant for Fe/K ($R^2 = 0.35$ (Figure 5b)), and insignificant for Fe/Ti ($R^2 = 0.13$ (Figure 5c)), although $R^2$ increases for Fe/Ti when the elemental contents from laminated and nonlaminated sediments are treated separately ($R^2 = 0.23$ and 0.20, respectively, not shown). This may indicate the effect of sedimentary nonhomogeneity on the measurements (see section 3.2).

[19] In the upper 15 m of core MD02-2503, the sediments are enriched in biogenic material (high Ca/Al ratio) and in the 15–47 m interval, they are enriched in terrigenous compounds (low Ca/Al ratio) (Figure 5a). In addition, the Ca/Al ratio undergoes high-amplitude and high-frequency variations in the upper 15 m, and low-amplitude and low-frequency variations in the 15–47 m interval. Absolute Fe/K and Fe/Ti ratios remain relatively constant along the core (Figures 5b and 5c). The slightly increasing up-core trends in relative Fe/K and Ca/Al ratios and decreasing trend in the relative Fe/Ti ratio in the upper 4 m of the core (not observed in the absolute contents) are probably attributable to higher water contents in the uppermost sediments.

## 6. Interpretation and Discussion

### 6.1. Changes in Magnetic Mineralogy

[20] High-SIRM/$\kappa$ layers in core MD02-2503 undergo a strong loss of $IRM_{9T}$ between 300 and 350°C (Figure 4c), which suggests the presence of authigenic ferrimagnetic sulfides such as greigite ($Fe_3S_4$) and/or pyrrhotite ($Fe_7S_8$) [*Roberts*, 1995]. The absence of a phase transition at 34 K in the low-temperature SIRM profiles [*Dekkers et al.*, 1989; *Rochette et al.*, 1990] is consistent with the dominance of greigite [*Roberts*, 1995] (Figure 4a). High-SIRM/$\kappa$ layers have high coercivity and high ARM unblocking fields, as indicated by high values of $H_c$, $H_{cr}$ and $ARM_{AF30mT}/ARM$ (Figure 4d). High ARM unblocking fields were already observed for greigite minerals [e.g., *Peters and Thompson*, 1998], and partial acquisition of gyroremanent magnetization could also account for high $ARM_{AF30mT}/ARM$ values [*Snowball*, 1997; *Sagnotti and Winkler*, 1999]. In core MD02-2503, alternating field (AF) demagnetization of the NRM of high-SIRM/$\kappa$ layers do not show evidence for gyroremanence acquisition (i.e., no increase of NRM during AF demagnetization (Figure 4e)). High-SIRM/$\kappa$ layers also have high saturation fields, as indicated by high values of HIRM and $H_{sat}$ (Figure 4d). This was never observed before for greigite minerals (A. Roberts, personal communication, 2009) and might be due to partial reoxidation of greigite minerals during storage and formation of a high saturation field mineral. The magnetic profiles for core MD02-2504 have less variability and fewer SIRM/$\kappa$ peaks, which

**Figure 4.** (a) Low-temperature IRM measurements: $IRM_{5T}$ (imposed at 300 K) measured during cooling (dark green thick curve) followed by warming (light green fine curve) in zero field. First derivatives of measurements realized during cooling (black dotted curve) indicate larger variations. (b) Magnetic properties of selected samples from core MD02-2503 at positions (green symbols) indicated on the SIRM/$\kappa$ profile. (c) High-temperature measurements: stepwise thermal demagnetization of $IRM_{9T}$. (d) Hysteresis measurements: hysteresis loops in saturation fields of ±1 T and demagnetization curves of the $IRM_{1T}$. Values of remanence saturation magnetization ($M_{rs}$), coercive force ($H_c$), and remanence coercivity ($H_{cr}$) are indicated on the hysteresis plots. (e) Alternative field (AF) demagnetization of natural remanent magnetization (NRM).
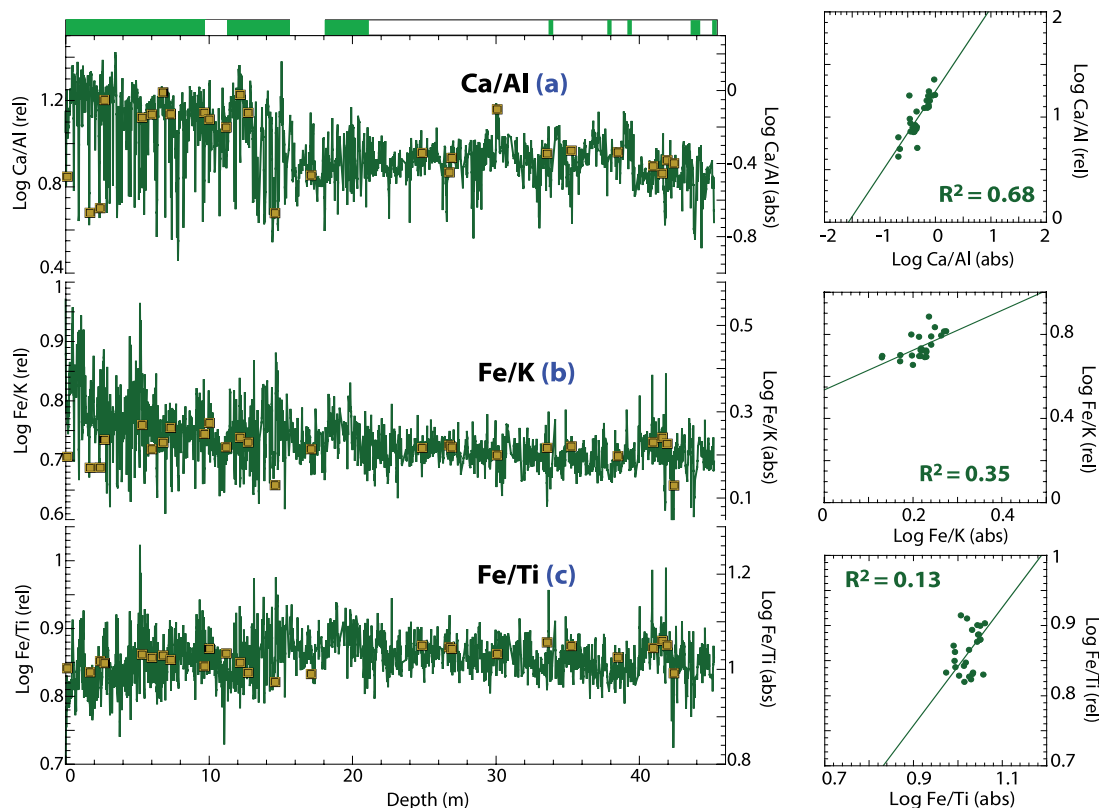
**Figure 5.** Depth variations of elemental concentrations in core MD02-2503. (a) The calcium over aluminum (Ca/Al) log ratio is an indicator of changes in biogenic/terrigenous material. Log ratios of (b) iron over potassium (Fe/K) and (c) iron over titanium (Fe/Ti) provide information about changes in mineralogy of the terrigenous fraction and/or diagenetic processes involving Fe (dissolution, migration, and recrystallization). Log ratios of the relative elemental contents (green curves) and the absolute contents (yellow squares, 26 samples) are compared with respect to depth and in scatterplots to estimate the reliability of the relative abundance data measured with the XRF core scanner [*Weltje and Tjallingii*, 2008]. The correlation is significant for Ca/Al and Fe/K but not for Fe/Ti (see text for details).

suggests that the presence of greigite is not as clear as in core MD02-2503 (Figure 3). Background sediments in core MD02-2503 seem to contain mainly magnetite, as suggested by the loss of $IRM_{9T}$ between 560 and 590°C and low $H_c$ and $H_{cr}$ values (Figures 4c and 4d) [*Hunt et al.*, 1995]. However, the presence of ultrafine (superparamagnetic) greigite minerals, though undetected by our analytical protocol, cannot be excluded [*Rowan et al.*, 2009].

### 6.2. Holocene Sedimentation Patterns

[21]   In the Holocene sequence of both cores, we identified a series of well-defined gray-colored layers, which are known in the SBB as gray layers (Figure 6a). They were interpreted by *Fleischer* [1972] as large flood deposits from the Santa Clara River. Because of their terrestrial origin and rapid deposition, these layers are rich in terrigenous material and poor in biogenic matter [*Fleischer*, 1972; *Thornton*, 1986]. This dominance in terrigenous matter in the gray layers (GL) is confirmed for core MD02-2503 by low Ca/Al ratios (Figure 6b). Some GL are evident in both cores, and may document large flood events or a modification of the sediment transportation route due to changes in oceanic

circulation (Figure 6a). GL thicker than 5 cm are associated with greigite enrichments (Figure 6c). A closer examination of changes in elemental and greigite contents across two GL indicates that (1) GL are characterized by low Ca/Al and Fe/K ratios (Figures 6e and 6f) and (2) the highest greigite content is recorded near or at the base of the GL (Figure 6g). The two GL detailed in Figure 6 are associated with high bioturbation indices, which indicates that they were deposited during periods of well-oxygenated BW [*Behl*, 1995]. Other GL are associated with varying bioturbation indices and no straightforward relationship can be determined between BW oxygenation and GL deposition.

[22]   Lower Ca/Al and Fe/K ratios reflect the characteristic enrichment of the GL in terrigenous compounds and their illite-dominated clay mineralogy [*Fleischer*, 1972]. Slightly higher Fe/K ratios (as well as Fe/Ti and Fe/Al ratios) just below the greigite-rich layers suggest Fe migration during early diagenesis (Figures 6f and 6g). The occurrence of postdepositional processes is further indicated by the presence of greigite at the base of the GL. As summarized by *Fu et al.* [2008], sedimentary greigite builds up through two main geochemical pathways, which both involve a mono-
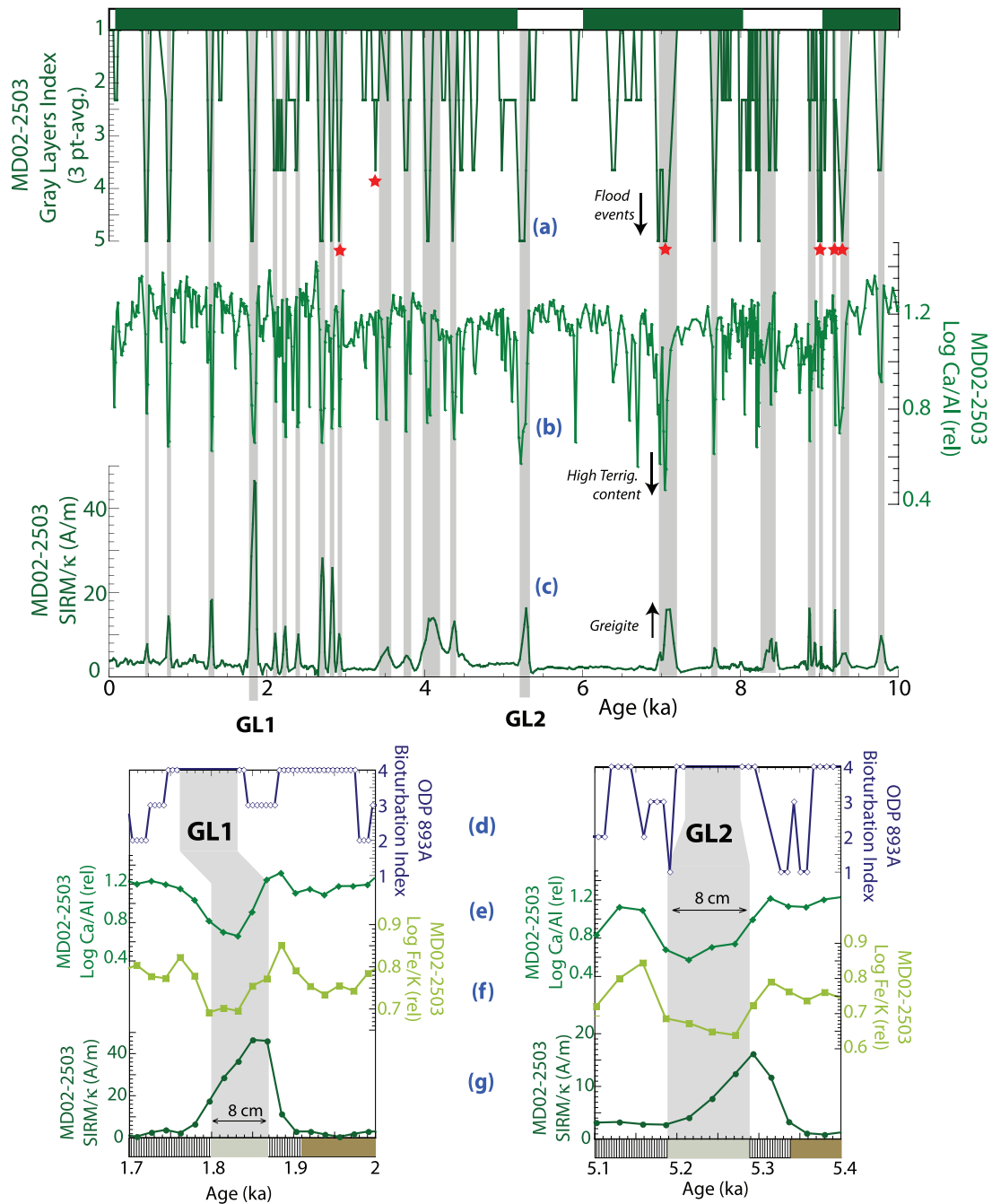
**Figure 6.** Sedimentary dynamics during the Holocene (0–10 ka). (a) Gray layers in core MD02-2503 (green curve) and at correlative depths in core MD02-2504 (red stars). Gray layer indices were established following *Behl* [1995]. (b) Relative variations of biogenic/terrigenous contents as indicated by the Ca/Al log ratio in core MD02-2503. (c) Greigite enrichments as indicated by SIRM/$\kappa$ and highlighted with gray shading. Detailed view of two greigite-rich gray layers: GL1 (1.7–2 ka) and GL2 (5.1–5.4 ka). (d) Bioturbation index for ODP Hole 893A [*Behl*, 1995], (e) Ca/Al log ratio, (f) Fe/K log ratio (which is an indicator of mineralogy of the terrigenous fraction and/or diagenetic enhancements), and (g) SIRM/$\kappa$, where peaks indicate greigite enrichments.

sulfide precursor (FeS). This FeS precursor forms during early diagenesis, by reaction of Fe(II) with $HS^-$. Both species can be released by iron oxides and sulfate reduction during anaerobic degradation of the organic matter. $HS^-$ can also form during anaerobic oxidation of methane deeper in the sediment column (i.e., at the sulfate-methane transition, section 2.2), and can then diffuse upward. Greigite can form as an intermediate species during the stepwise con-
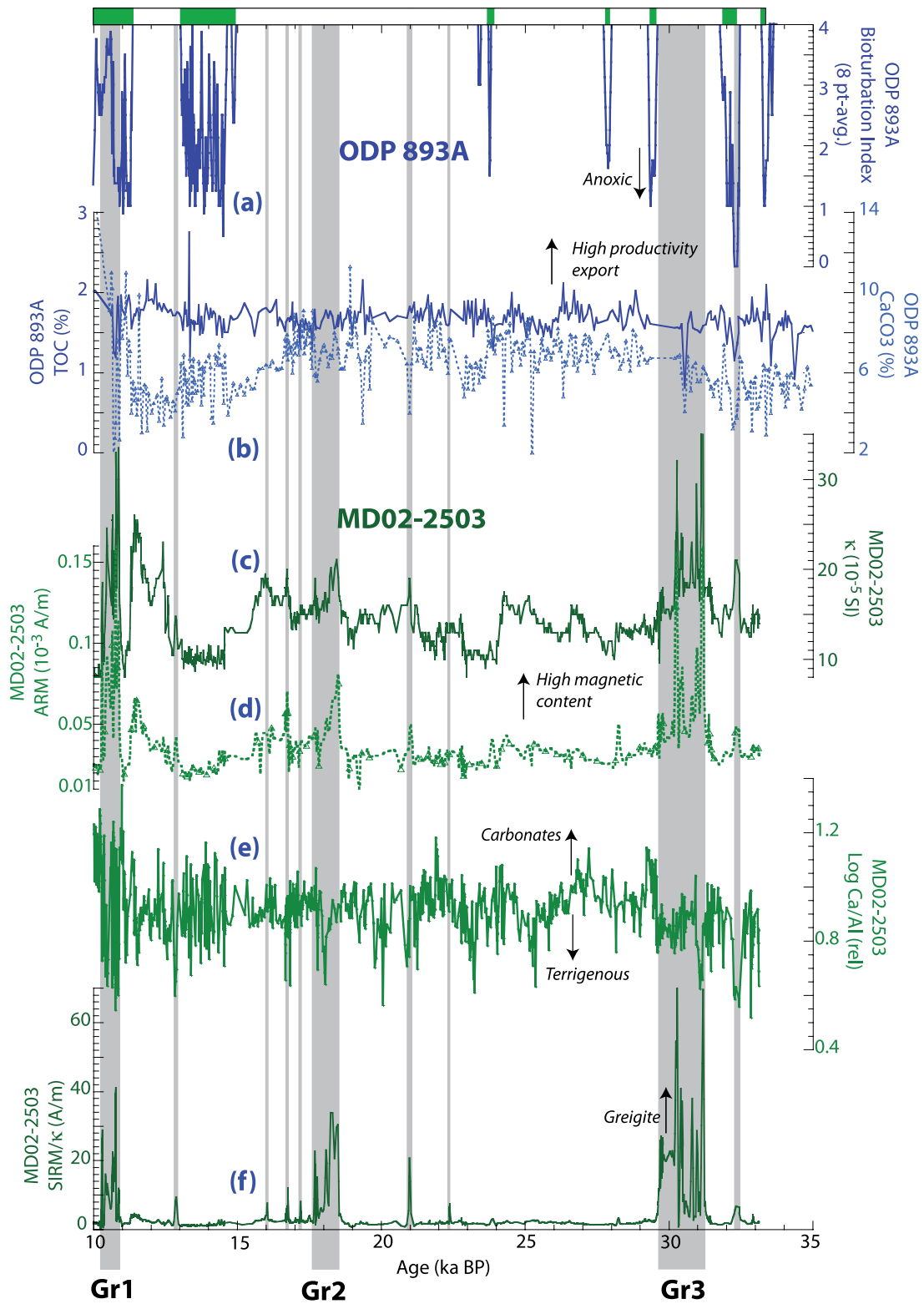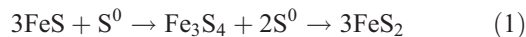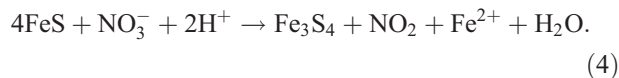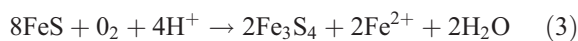
**Figure 7**

version of FeS into pyrite (FeS$_2$) [*Berner*, 1984; *Sweeney and Kaplan*, 1973; *Hunger and Benning*, 2007]:

$$3FeS + S^0 \rightarrow Fe_3S_4 + 2S^0 \rightarrow 3FeS_2 \qquad (1)$$

$$3FeS + HS^- \rightarrow Fe_3S_4 + 2HS^- + 2H^+ \rightarrow 3FeS_2 + 4H^+. \qquad (2)$$

As seen from these equations, sufficient amounts of HS$^-$ and S$^0$ (formed by partial reoxidation of FeS or HS$^-$) are needed to complete the conversion of FeS into pyrite. Because of low organic content in the GL, Fe(III) and sulfate reduction was probably less intense than in the background sediments, which led to a lower production of HS$^-$ and S$^0$ [*Ivanochko and Pedersen*, 2004]. Because of high terrigenous content in the GL, the ratio of reactive iron over HS$^-$ was probably higher in these layers than in the background sediments. A shortage of HS$^-$ with regard to the amount of reactive iron would then have favored formation and preservation of greigite because of its incomplete conversion into pyrite [*Kao et al.*, 2004]. The fact that the greigite formed at the base of the GL suggests that upward diffusing HS$^-$ reacted with downward diffusing Fe$^{2+}$ (equations (1) and (2)) or directly with the iron oxides or with FeS, to form greigite [*Berner*, 1984; *Poulton et al.*, 2004; *Fu et al.*, 2008]. Greigite is observed only in association with GL thicker than 5 cm, which suggests that the ratio of reactive Fe over HS$^-$ in thinner GL was not sufficient to prevent a complete conversion of greigite into pyrite.

[23] Greigite can also form as a product of FeS oxidation by O$_2$ or NO$_3^-$ [*Wilkin and Barnes*, 1997; *Schippers and Jørgensen*, 2002]:

$$8FeS + 0_2 + 4H^+ \rightarrow 2Fe_3S_4 + 2Fe^{2+} + 2H_2O \qquad (3)$$

$$4FeS + NO_3^- + 2H^+ \rightarrow Fe_3S_4 + NO_2 + Fe^{2+} + H_2O. \qquad (4)$$

The formation of greigite following this pathway seems less likely since the sediments at the base of the GL might be oxygen- and nitrate-free because of rapid upward migration of the redox front. Deposition of the GL was probably too fast to allow downward diffusion of O$_2$ and NO$_3^-$ into the base of the layer (like during "burn-down" events

[*Thomson et al.*, 1996]). Repeated deposition of GL during the Holocene probably created a highly dynamic sedimentary system (in terms of sedimentation rate and composition), which resulted in nonsteady state diagenesis that favored preservation of metastable sulfide minerals [*Zabel and Schulz*, 2001; *Kasten et al.*, 2003; *Larrasoaña et al.*, 2003].

### 6.3. Glacial Sedimentation Patterns

[24] During the sea level low stand of the last glacial, the mouths of the Ventura and Santa Clara rivers were shifted toward the adjacent Santa Monica Basin [*Behl*, 1995]. Thus, the glacial sediments do not contain GL. Yet, three thick greigite-rich layers are evident during the last glacial (Figure 7f): at 10–11 ka (Gr1, ∼2 m thick), 16–19 ka (Gr2, ∼5 m thick) and 29–31 ka (Gr3, ∼3 m thick). These layers occur in nonlaminated sediments containing benthic foraminifera that indicate well-oxygenated bottom waters (i.e., with high bioturbation indices (Figure 7a)) [*Behl and Kennett*, 1996]. The presence of an oxygen-rich water mass along the Californian margin during most of the glacial has been confirmed by several studies [*van Geen et al.*, 1996; *Keigwin*, 1998].

[25] Greigite-rich layers Gr1, Gr2 and Gr3, like their Holocene equivalents, formed within biogenic-poor and terrigenous-rich sediments. Greigite-bearing sediments deposited during the glacial have (1) low contents of CaCO$_3$, organic carbon (Figure 7b) [*Gardner and Dartnell*, 1995] and opal (R. Thunell, unpublished data, 2000), (2) high concentrations of magnetic minerals (high $\kappa$ and ARM (Figures 7c and 7d)) and (3) high ratios of terrigenous/biogenic carbonates, as indicated by low Ca/Al ratios (Figure 7e). We suggest that the mechanism triggering greigite formation is similar to that described for the Holocene sequence: higher contents of reactive Fe (due to higher contents of iron (oxyhydr)oxides) and lower rates of sulfate and Fe(III) reduction (due to lower contents of organic matter), which led to a Fe/HS$^-$ ratio favoring the incomplete conversion of FeS into pyrite [*Kao et al.*, 2004]. Preservation of the meter-thick greigite-bearing layers might have been favored by the high Fe/organic matter ratios of the glacial sediments. Although not noticed in the age/depth transformation nor in the core description, the presence of the greigite-rich layers suggests faster deposition in these specific sedimentary intervals (Figure 2).

[26] Higher $\kappa$ values in core MD02-2504 (i.e., at 400 m water depth) at times of greigite formation in core MD02-2503 (i.e., in the deep part of the basin) indicate that sediments deposited at shallower depth also were also enriched in magnetic minerals in layers Gr1, Gr2 and Gr3 (Figure 8b). This suggests that sediments deposited in the SBB at these times were enriched in terrigenous material.

---

**Figure 7.** Sedimentary dynamics during the glacial period (10–35 ka) in core MD02-2503. (a) Bioturbation index for ODP Hole 893A, which is a proxy for bottom water oxygenation [*Behl*, 1995]. (b) Indices for export productivity in ODP Hole 893A: total organic carbon (TOC) (solid curve) and CaCO$_3$ (dashed curve) contents [*Gardner and Dartnell*, 1995]. Magnetic mineral content in core MD02-2503 as indicated by (c) magnetic susceptibility ($\kappa$) and (d) ARM. (e) Biogenic/ terrigenous contents in core MD02-2503 as indicated by the Ca/Al log ratio. (f) SIRM/$\kappa$ is an indicator of greigite enrichments. The greigite-bearing layers are highlighted with gray shading and are labeled Gr1 (10.2–11 ka), Gr2 (17.6–18.5 ka), and Gr3 (29.6–31.3 ka).
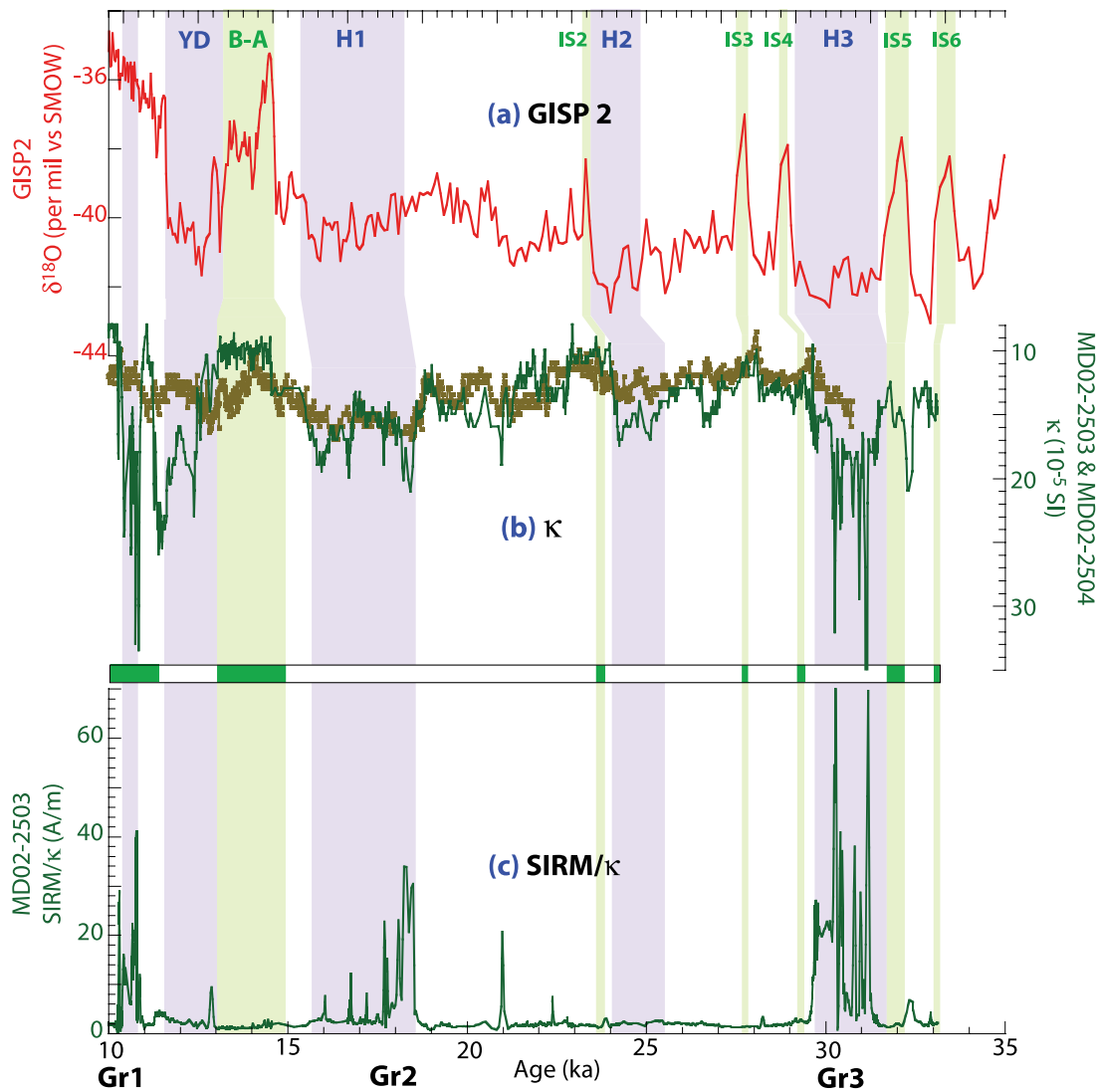
**Figure 8.** Paleoclimatic features of the glacial period in the Santa Barbara Basin (10−35 ka). (a) Atmospheric temperatures over Greenland as indicated by $\delta^{18}O$ in the GISP2 ice core [*Grootes and Stuiver*, 1997]. (b) Terrigenous inputs in core MD02-2503 (green) and MD02-2504 (brown) as indicated by the low field magnetic susceptibility ($\kappa$). (c) Greigite enrichments in core MD02-2503, as indicated by SIRM/$\kappa$. Climatic events of the last glacial period are indicated at the top of the plot: Heinrich events, H1, H2, and H3; Younger Dryas, YD; Blling-Allerd, B-A; and interstadials, IS2, IS3, IS4, IS5, and IS6.

On a glacial/interglacial scale, changes in sediment accumulation rate are mainly controlled by changes in terrigenous inputs [*Dean et al.*, 2006]. We assume that this is also true at millennial scale and we use variations in magnetic mineral content to trace changes in terrigenous input (Figure 8b). Comparison of the magnetic record for core MD02-2503 with a record of climatic changes in the northern hemisphere (GISP2 [*Grootes and Stuiver*, 1997]) indicates that greigite-bearing layer Gr1 occurred at the time of preboral drift ice event 7 and that greigite layers Gr2 and Gr3 occurred just before or at the time of Heinrich events (HE) 1 and 3 (Figures 8a and 8c). The absence of greigite-bearing layer in association with HE2 might be due to a ratio Fe/HS$^-$ that was insufficient to preserve greigite, although the terrigenous input was higher at this time

(Figures 7 and 8). HE are calving events of the Laurentide Ice Sheet that resulted in abrupt and massive iceberg surges and fresh water invasions into the North Atlantic [*Bond et al.*, 1992, 2001] and North Pacific [*Kotilainen and Shackleton*, 1995; *Hendy and Cosma*, 2008]. These events had consequences for both global climate and sea level [e.g., *Yokoyama et al.*, 2001; *Voelker and workshop participants*, 2002]. However, previous oceanic and climatic records from the SBB mainly contain Dansgaard-Oeschger (DO) type fluctuations and do not contain HE signatures [*Behl and Kennett*, 1996; *Heusser*, 1998; *Hendy and Kennett*, 1999]. Even the magnetic record of terrigenous input to the nearby Tanner Basin contains DO-type fluctuations [*Heider et al.*, 2001]. In the SBB, increased terrigenous input during the HE (Figure 8b) can be

attributed either to climate-induced changes in erosion rates on the continent or to remobilization of shelf sediments during sea level variations. Cold conditions have been documented on the Californian coast during the HE, through glacier advances in the Sierra Nevada [*Phillips et al.*, 1996], low lake levels [*Benson et al.*, 1998] and vegetation changes [*Koehler and Anderson*, 1995]. These conditions could have favored increased sediment delivery to the SBB due to decreased vegetation cover, or to enhanced efficiency of sediment transport by winds or rivers. In addition, sea level variations within the reduced area of the basin could have triggered remobilization of shelf and slope sediments. Recently, several studies have documented significant sea level variations during MIS 3, with amplitudes ranging from 10 to 30 m [e.g., *Arz et al.*, 2007]. They seem to occur just before or during the HE [*Rohling et al.*, 2008], and could have induced redeposition of slope sediments in the deepest parts of the basin.

## 7. Conclusions

[27] Magnetic and geochemical data with a temporal resolution of ∼15 years from two cores collected in the Santa Barbara Basin enable assessment of the influence of varying terrigenous input on the dynamics of nonsteady state diagenesis. The magnetic record of the core from the deepest part of the basin has recurrent enrichments in the ferrimagnetic iron sulfide, greigite ($Fe_3S_4$), which has been identified by its typical magnetic signature (high ratio SIRM/$\kappa$, demagnetization at 300°C [*Roberts*, 1995]).

[28] Holocene sediments from the Santa Barbara Basin contain a series of centimeter-thick greigite-bearing layers (Figure 6). These layers occur at the base of rapidly deposited flood sediments (called gray layers), which have high terrigenous content and low organic matter content [*Fleischer*, 1972]. The high Fe content and low organic

contents within these layers may have induced a shortage of HS⁻ with regard to the amount of Fe and prevented the complete conversion of monosulfides into pyrite, thus leading to greigite formation [*Kao et al.*, 2004]. The nonsteady state diagenesis generated by the repeated deposition of near-instantaneous gray layers appear to have favored greigite preservation within specific intervals.

[29] Glacial sediments contain a few meter-thick greigite-bearing layers (Figure 7). These layers occur in terrigenous-rich and biogenic-poor sediments, in which the Fe/organic matter ratio also appears to have favored greigite preservation, as is the case in the Holocene gray layers. Layers enriched in magnetic mineral content in a core collected at shallower depth, which fall at times of greigite-bearing layers, indicate that these were intervals of enhanced terrigenous input at basin scale (Figure 8). The thick greigite-bearing layers occur at the time of Heinrich events, which were massive iceberg release in the North Atlantic (Figure 8). Therefore, in contrast to climatic records previously established in the Santa Barbara Basin, the terrigenous input appears to respond to climatic or sea level variations associated with Heinrich events.

## References

Arz, H., F. Lamy, A. Ganopolski, N. Nowaczyk, and J. Paetzold (2007), Dominant Northern Hemisphere control over millennial-scale glacial sea-level variability, *Quat. Sci. Rev.*, *26*, 312–321.

Barnes, R. O., and E. G. Goldberg (1976), Methane production and consumption in anoxic marine sediments, *Geology*, *4*, 297–300.

Beaufort, L., T. Pedersen, M. Machain-Castillo, and the cruise participants (2002), Marges Ouest Nord Américaines (MONA) cruise report, *Rep. MD126-IMAGESVIII*, Inst. Paul Emile Victor, Plouzané, France.

Behl, R. J. (1995), Sedimentary facies and sedimentology of the Late Quaternary Santa Barbara Basin, Site 893, *Proc. Ocean Drill. Program Sci. Results*, *146*, 295–308.

Behl, R. J., and J. P. Kennett (1996), Brief interstadial events in the Santa Barbara Basin, NE Pacific, during the past 60 kyr, *Nature*, *379*, 243–246.

Benson, L. V., H. M. May, R. C. Antweiler, T. I. Brinton, M. Kashgarian, J. Smoot, and S. Lund (1998), Continuous lake-sediment records of glaciation in the Sierra Nevada between 52,600 and 12,500 ¹⁴C yr B.P., *Quat. Res.*, *50*, 113–127.

Berner, R. A. (1984), Sedimentary pyrite formation: An update, *Geochim. Cosmochim. Acta*, *48*, 605–615.

Bloemendal, J., J. King, A. Hunt, P. de Menocal, and A. Hayashida (1993), Origin of the sedimentary magnetic record at Ocean Drilling Program sites on the Owen ridge, western Arabian Sea, *J. Geophys. Res.*, *98*, 4199–4219.

Bond, G., et al. (1992), Evidence of massive discharges of icebergs into the North Atlantic Ocean during the last glacial period, *Nature*, *360*, 245–249.

Bond, G., B. Kromer, J. Beer, R. Muscheler, M. N. Evans, W. Showers, S. Hoffmann, R. Lotti-Bond, I. Hajdas, and G. Bonani (2001), Persistent solar influence on North Atlantic climate during the Holocene, *Science*, *294*, 2130–2136.

Bull, D., and A. E. S. Kemp (1995), Composition and origin of laminae in Late Quaternary and Holocene sediments from the Santa Barbara Basin, *Proc. Ocean Drill. Program Sci. Results*, *146*, 77–87.

California Cooperative Oceanic Fisheries Investigations (CalCOFI) (2005), CalCOFI cruise 0501 physical, chemical and biological data,

*Data Rep. 07-03*, Scripps Inst. of Oceanogr., Univ. of Calif., San Diego, La Jolla.

California Cooperative Oceanic Fisheries Investigations (CalCOFI) (2007a), CalCOFI cruise 0704 hydrographic report, data report, Scripps Inst. of Oceanogr., Univ. of Calif., San Diego, La Jolla.

California Cooperative Oceanic Fisheries Investigations (CalCOFI) (2007b), CalCOFI cruise 0711 hydrographic report, data report, Scripps Inst. of Oceanogr., Univ. of Calif., San Diego, La Jolla.

Cannariato, K. G., J. P. Kennett, and R. J. Behl (1999), Biotic response to Late Quaternary rapid climate switches in Santa Barbara Basin: Ecological and evolutionary implications, *Geology*, *27*, 63–66.

Conil, S., and A. Hall (2006), Local regimes of atmospheric variability: A case study of southern California, *J. Clim.*, *19*, 4308–4325, doi:10.1175/JCLI3837.1.

Conkright, M. E., R. A. Locarnini, H. E. Garcia, T. D. O'Brien, T. P. Boyer, C. Stephens, and J. I. Antonov (2002), World Ocean Atlas 2001: Objective analyses, data statistics, and figures CD-ROM documentation, *Int. Rep. 17*, Natl. Oceanogr. Data Cent., Silver Spring, Md.

Dean, W. E., Y. Zheng, J. D. Ortiz, and A. van Geen (2006), Sediment Cd and Mo accumulation in the oxygen-minimum zone off western Baja California linked to global climate over the past 52 kyr, *Paleoceanography*, *21*, PA4209, doi:10.1029/2005PA001239.

Dekkers, M. J., J.-L. Mattéi, G. Fillion, and P. Rochette (1989), Grain-size dependence of the magnetic behavior of pyrrhotite during its low-temperature transition at 34 K, *Geophys. Res. Lett.*, *16*, 855–858.

Emmer, E., and R. Thunell (2000), Nitrogen isotope variations in Santa Barbara Basin sediments: Implications for denitrification in the eastern tropical North Pacific during the last 50,000 years, *Paleoceanography*, *15*, 377–387.

Fleischer, P. (1972), Mineralogy and sedimentation history, Santa Barbara Basin, California, *J. Sediment. Petrol.*, *42*, 49–58.

Fu, Y., T. von Dobeneck, C. Franke, D. Heslop, and S. Kasten (2008), Rock magnetic identification and geochemical process models of greigite formation in Quaternary marine sediments from the Gulf of Mexico (IODP Hole U1319A), *Earth Planet. Sci. Lett.*, *275*, 233–245.

Gardner, J. V., and P. Dartnell (1995), Centennial-scale Late Quaternary stratigraphies of carbonate and organic carbon from Santa Barbara Basin, Hole 893A and their paleoceanographic significance, *Proc. Ocean Drill. Program Sci. Results*, *146*, 103–124.

Grootes, P. M., and M. Stuiver (1997), Oxygen 18/16 variability in Greenland snow and ice with $10^{-3}$- to $10^{-5}$-year time resolution, *J. Geophys. Res.*, *102*, 26,455–26,470.

Heider, F., J. M. Bock, I. Hendy, J. P. Kennett, J. Matzka, and J. Schneider (2001), Latest Quaternary rock magnetic record of climatic and oceanic change, Tanner Basin, California borderland, *Geol. Soc. Am. Bull.*, *113*, 346–359.

Hendy, I. L., and T. Cosma (2008), Vulnerability of the Cordilleran Ice Sheet to iceberg calving during the Late Quaternary rapid climate change events, *Paleoceanography*, *23*, PA2101, doi:10.1029/2008PA001606.

Hendy, I. L., and J. P. Kennett (1999), Latest Quaternary North Pacific surface-water responses imply atmosphere-driven climate instability, *Geology*, *27*, 291–294.

Hendy, I. L., J. P. Kennett, E. B. Roark, and B. L. Ingram (2002), Apparent synchroneity of submillennial scale climate events between Greenland and Santa Barbara Basin, California from 30–10 ka, *Quat. Sci. Rev.*, *21*, 1167–1184.

Heusser, L. (1998), Direct correlation of millennial-scale changes in western North American vegetation and climate with changes in the California Current system over the past ~60 kyr, *Paleoceanography*, *13*, 252–262.

Hill, T. M., J. P. Kennett, D. K. Pack, R. J. Behl, C. Robert, and L. Beaufort (2006), Pre-Bølling warming in Santa Barbara Basin, California: Surface and intermediate waters record of early deglacial warmth, *Quat. Sci. Rev.*, *25*, 2835–2845.

Hunger, S., and L. G. Benning (2007), Greigite: A true intermediate on the polysulfide pathway to pyrite, *Geochem. Trans.*, *8*, doi:10.1186/1467-4866-8-1.

Hunt, C. P., B. M. Moskowitz, and S. K. Banerjee (1995), Magnetic properties of rocks and minerals, in *Rock Physics and Phase Relations: A Handbook of Physical Constants*, *AGU Ref. Shelf*, vol. 3, edited by T. J. Ahrens, pp. 189–204, AGU, Washington, D. C.

Ingram, B. L., and J. P. Kennett (1995), Radiocarbon chronology and planktonic-benthic foraminiferal ^{14}C age differences in Santa Barbara Basin sediments, Hole 893A, *Proc. Ocean Drill. Program Sci. Results*, *146*, 19–27.

Ivanochko, T. S., and T. F. Pedersen (2004), Determining the influences of Late Quaternary ventilation and productivity variations on Santa Barbara Basin sedimentary oxygenation: A multi-proxy approach, *Quat. Sci. Rev.*, *23*, 467–480.

Kao, S.-J., C.-S. Horng, A. P. Roberts, and K.-K. Liu (2004), Carbon-sulfur-iron relationships in sedimentary rocks from southwestern Taiwan: Influence of geochemical environment on greigite and pyrrhotite formation, *Chem. Geol.*, *203*, 153–168.

Kasten, S., M. Zabel, V. Heuer, and C. Hensen (2003), Processes and signals of nonsteady-state diagenesis in deep-sea sediments and their pore waters, in *The South Atlantic in the Late Quaternary: Reconstruction of Material Budgets and Current Systems*, edited by G. Wefer, S. Mulitza, and V. Ratmeyer, pp. 431–459, Springer, Berlin.

Keigwin, L. D. (1998), Glacial-age hydrography of the far northwest Pacific Ocean, *Paleoceanography*, *13*, 323–339.

Koehler, P. A., and R. S. Anderson (1995), Thirty thousand years of vegetation changes in the Alabama Hills, Owens Valley, California, *Quat. Res.*, *43*, 238–248.

Köhler, C. M., D. Heslop, M. J. Dekkers, W. Krijgsman, D. J. J. van Hinsbergen, and T. von Dobeneck (2008), Tracking provenance change during the late Miocene in the eastern Mediterranean using geochemical and environmental magnetic parameters, *Geochem. Geophys. Geosyst.*, *9*, Q12018, doi:10.1029/2008GC002127.

Kotilainen, A. T., and N. J. Shackleton (1995), Rapid climate variability in the North Pacific Ocean during the past 95,000 years, *Nature*, *377*, 323–326.

Kuwabara, J. S., A. van Geen, D. C. McCorkle, and J. M. Berhnard (1999), Dissolved sulfide distributions in the water column and sediment pore waters of the Santa Barbara Basin, *Geochim. Cosmochim. Acta*, *63*, 2199–2209.

Larrasoaña, J. C., A. P. Roberts, J. S. Stoner, C. Richter, and R. Wehausen (2003), A new proxy for bottom-water ventilation in the eastern Mediterranean based on diagenetically controlled magnetic properties of sapropel-bearing sediments, *Palaeogeogr. Palaeoclimatol. Palaeoecol.*, *190*, 221–242.

Leslie, B. W., S. P. Lund, and D. E. Hammond (1990), Rock magnetic evidence for the dissolution and authigenic growth of magnetic minerals within anoxic sediments of the California continental borderland, *J. Geophys. Res.*, *95*, 4437–4452.

Moreno, E., N. Thouveny, D. Delanghe, N. McCave, and N. J. Shackleton (2002), Climatic and oceanographic changes in the northeast Atlantic reflected by magnetic properties of sediments deposited on the Portuguese margin during the last 340 ka, *Earth Planet. Sci. Lett.*, *202*, 465–480.

Paillard, D., J. Labeyrie, and F. Yiou (1996), Macintosh program performs time-series analysis, *Eos Trans. AGU*, *77*, 379.

Peters, C., and R. Thompson (1998), Magnetic identification of selected natural iron oxides and sulphides, *J. Magn. Magn. Mater.*, *183*, 365–374.

Phillips, F. M., M. G. Zreda, L. V. Benson, M. A. Plummer, D. Elmore, and P. Sharma (1996), Chronology for fluctuations in late Pleistocene Sierra Nevada glaciers and lakes, *Science*, *274*, 749–751.

Pospelova, V., T. F. Pedersen, and A. de Vernal (2006), Dinoflagellate cysts as indicators of climatic and oceanographic changes during the past 40 kyr in the Santa Barbara Basin, southern California, *Paleoceanography*, *21*, PA2010, doi:10.1029/2005PA001251.

Poulton, S. W., M. D. Krom, and R. Raiswell (2004), A revised scheme for the reactivity of iron (oxyhydr)oxide minerals towards dissolved sulfide, *Geochim. Cosmochim. Acta*, *68*, 3703–3715.

Rack, F., E. A. Heise, and R. Stein (1995), Magnetic susceptibility and physical properties of sediment cores from Site ODP 893, Santa Barbara Basin: Records of sediment diagenesis or of paleoclimatic and paleoceanographic change?, *Proc. Ocean Drill. Program Sci. Results*, *146*, 19–27.

Reimers, C. E., C. Lange, M. Tabak, and J. M. Bernhard (1990), Seasonal spillover and varve formation in the Santa Barbara Basin, California, *Limnol. Oceanogr.*, *35*, 1577–1585.

Reimers, C. E., K. C. Ruttenberg, D. E. Canfield, M. B. Christiansen, and J. B. Martin (1996), Porewater pH and authigenic phases formed in the uppermost sediments of the Santa Barbara Basin, *Geochim. Cosmochim. Acta*, *60*, 4037–4057.

Richter, T. O., S. van der Gaast, R. Koster, A. Vaars, R. Gieles, H. C. de Stigter, H. de Haas, and T. C. E. van Weering (2006), The Avaatech XRF core scanner: Technical description and applications to NE Atlantic sediments, in *New Techniques in Sediment Core Analysis*, edited by R. G. Rothwell, *Geol. Soc. Spec. Publ.*, *267*, 39–50.

Roberts, A. P. (1995), Magnetic properties of sedimentary greigite ($Fe_3S_4$), *Earth Planet. Sci. Lett.*, *134*, 227–236.

Roberts, A. P., and R. Weaver (2005), Multiple mechanisms of remagnetization involving sedimentary greigite ($Fe_3S_4$), *Earth Planet. Sci. Lett.*, *231*, 263–277.

Rochette, P., G. Fillion, J.-L. Mattéi, and M. J. Dekkers (1990), Magnetic transition at 30–34 kelvin in pyrrhotite: Insight into a widespread occurrence of this mineral in rocks, *Earth Planet. Sci. Lett.*, *98*, 319–328.

Rochette, P., F. Vadeboin, and L. Clochard (2001), Rock magnetic applications of Halbach cylinders, *Phys. Earth Planet. Inter.*, *126*, 109–117.

Rohling, E. J., K. Grant, C. Hemleben, M. Kucera, A. P. Roberts, I. Schmeltzer, H. D. Schulz, M. Siccha, M. Siddall, and G. Trommer (2008), New constraints on the timing of sea level fluctuations during early to middle marine isotope stage 3, *Paleoceanography*, *23*, PA3219, doi:10.1029/2008PA001617.

Rowan, C. J., A. P. Roberts, and T. Broadbent (2009), Reductive diagenesis, magnetite dissolution, greigite growth and paleomagnetic smoothing in marine sediments: A new view, *Earth Planet. Sci. Lett.*, *277*, 223–235.

Sagnotti, L., and A. Winkler (1999), Rock magnetism and paleomagnetism of greigite-bearing mudstones in the Italian peninsula, *Earth Planet. Sci. Lett.*, *165*, 67–80.

Schippers, A., and B. B. Jørgensen (2002), Biogeochemistry of pyrite and iron sulfide oxidation in marine sediments, *Geochim. Cosmochim. Acta*, *66*, 85–92.

Snowball, I. F. (1997), Gyroremanent magnetization and the magnetic properties of greigite-bearing clays in southern Sweden, *Geophys. J. Int.*, *129*, 624–636.

Soutar, A., and P. A. Crill (1977), Sedimentation and climatic patterns in the Santa Barbara Ba-

sin during the 19th and 20th centuries, *Geol. Soc. Am. Bull.*, *88*, 1161–1172.

Sweeney, R. E., and I. R. Kaplan (1973), Pyrite framboid formation: Laboratory synthesis and marine sediments, *Econ. Geol.*, *68*, 618–634.

Thomson, J., N. C. Higgs, and S. Colley (1996), Diagenetic redistributions of redox-sensitive elements in northeast Atlantic glacial/interglacial transition sediments, *Earth Planet. Sci. Lett.*, *139*, 365–377.

Thornton, S. E. (1986), Origin of mass flow sedimentary structures in hemipelagic basin deposits: Santa Barbara Basin, California borderland, *Geo Mar. Lett.*, *6*, 15–19.

van Geen, A., R. G. Fairbanks, P. Dartnell, M. McGann, J. V. Gardner, and M. Kashgarian (1996), Ventilation changes in the northeast Pacific during the last deglaciation, *Paleoceanography*, *11*, 519–528.

Voelker, A. H. L. and workshop participants (2002), Global distribution of centennial-scale records for marine isotope stage (MIS) 3: A database, *Quat. Sci. Rev.*, *21*, 1185–1212.

Weeks, R., C. Laj, L. Endignoux, M. Fuller, A. Roberts, R. Manganne, E. Blanchard, and W. Goree (1993), Improvements in long-core measurement techniques: Applications in palaeomagnetism and palaeoceanography, *Geophys. J. Int.*, *114*, 651–662, doi:10.1111/j.1365-246X.1993.tb06994.x.

Weltje, G.-J., and R. Tjallingii (2008), Calibration of XRF core scanners for quantitative geochemical logging of sediment cores: Theory and application, *Earth Planet. Sci. Lett.*, *274*, 423–438.

Westerling, A. L., D. R. Cayan, T. J. Brown, B. L. Hall, and L. G. Riddle (2004), Climate, Santa Ana winds and autumn wildfires in southern California, *Eos Trans. AGU*, *85*, 289–296, doi:10.1029/2004EO310001.

Wien, K., D. Wissmann, M. Kölling, and H. D. Schulz (2005), Fast application of X-ray fluorescence spectrometry aboard ship: How good is the new portable Spectro Xepos analyser?, *Geo Mar. Lett.*, *25*, 248–264.

Wilkin, R. T., and H. L. Barnes (1997), Formation processes of framboidal pyrite, *Geochim. Cosmochim. Acta*, *61*, 323–339.

Yokoyama, Y., T. M. Esat, and K. Lambeck (2001), Coupled climate and sea-level changes deduced from Huon Peninsula coral terraces of the last ice age, *Earth Planet. Sci. Lett.*, *193*, 579–587.

Zabel, M., and H. D. Schulz (2001), Importance of submarine landslides for non-steady state conditions in pore water systems: Lower Zaire (Congo) deep-sea fan, *Mar. Geol.*, *176*, 87–89.

———————————

C. L. Blanchet, Leibnitz Institute of Marine Sciences at University of Kiel (IFM-GEOMAR), East Shore Campus, Wischhofstrasse 1-3, D-24148 Kiel, Germany. (cblanchet@ifm-geomar.de)

N. Thouveny and L. Vidal, CEREGE, Université Paul Cézanne, Europole de l'Arbois, F-13445 Aix en Provence Cedex 4, France.